Intermittent AGN episodes drive outflows with a large spread of observable loading factors

Kastytis Zubovas [1,2]★ and Emanuele Nardini [3,4]

[1]*Center for Physical Sciences and Technology, Saulėtekio al. 3, Vilnius LT-10257, Lithuania*
[2]*Vilnius University Observatory, Saulėtekio al. 3, Vilnius LT-10257, Lithuania*
[3]*Dipartimento di Fisica e Astronomia, Università di Firenze, via G. Sansone 1, I-50019 Sesto Fiorentino, Firenze, Italy*
[4]*INAF - Osservatorio Astrofisico di Arcetri, Largo Enrico Fermi 5, I-50125 Firenze, Italy*

ABSTRACT
The properties of large-scale galactic outflows, such as their kinetic energy and momentum rates, correlate with the luminosity of the active galactic nucleus (AGN). This is well explained by the wind-driven outflow model, where a fraction of the AGN luminosity drives the outflow. However, significant departures from these correlations have been observed in a number of galaxies. This may happen because AGN luminosity varies on a much shorter time-scale ($\sim 10^4$–10^5 yr) than outflow properties do ($\sim 10^6$ yr). We investigate the effect of AGN luminosity variations on outflow properties using 1D numerical simulations. This effect can explain the very weak outflow in PDS 456: if its nucleus is currently much brighter than the long-term average luminosity, the outflow has not had time to react to this luminosity change. Conversely, the outflow in Mrk 231 is consistent with being driven by an almost continuous AGN, while IRAS F11119+3257 represents an intermediate case between the two. Considering a population of AGN, we find that very low momentum loading factors $\dot{p}_{\rm out} < L_{\rm AGN}/c$ should be seen in a significant fraction of objects – up to 15 per cent depending on the properties of AGN variability and galaxy gas fraction. The predicted distribution of loading factors is consistent with the available observational data. We discuss how this model might help constrain the duty cycles of AGN during the period of outflow inflation, implications for multiphase, and spatially distinct outflows, and suggest ways of improving AGN prescriptions in numerical simulations.

Key words: accretion, accretion discs – galaxies: active – quasars: general.

1 INTRODUCTION

Supermassive black holes (SMBHs) are known to exist in the majority of, if not all, galaxies (Heckman & Best 2014). For a small fraction of its lifetime, each SMBH accretes material rapidly and becomes visible as an active galactic nucleus (AGN). Many AGN show evidence of fast, quasi-relativistic winds with velocities $v_{\rm w} \sim 0.1c$ that carry a significant fraction $\eta \sim 0.05$ of the AGN luminosity as kinetic power (Pounds et al. 2003; Tombesi et al. 2014). These winds are believed to drive large-scale outflows that sweep gas out of galaxies, quenching their star formation (Feruglio et al. 2010; Sturm et al. 2011; Tombesi et al. 2015). This mechanism is responsible for the high-mass cutoff in the galaxy mass function, as shown in many semi-analytical (e.g. Bower et al. 2006; Croton et al. 2006) and hydrodynamical simulations that test the effects of AGN feedback (e.g. Sijacki et al. 2007; Puchwein & Springel 2013; Dubois et al. 2014; Vogelsberger et al. 2014; Schaye et al. 2015; Tremmel et al. 2019).

Many outflow properties, such as the mass flow rate $\dot{M}_{\rm out}$, velocity $v_{\rm out}$, momentum rate $\dot{p}_{\rm out} = \dot{M}_{\rm out} v_{\rm out}$, and kinetic energy rate $\dot{E}_{\rm out} = \dot{M}_{\rm out} v_{\rm out}^2 / 2$ correlate with the luminosity of the driving AGN (Cicone et al. 2014; Fiore et al. 2017; González-Alfonso et al.

2017; Fluetsch et al. 2019; Lutz et al. 2020). These correlations have been predicted by the wind-driven outflow model (King 2010a; Zubovas & King 2012; King & Pounds 2015), which is based on the assumption that large-scale outflows are inflated when the SMBH mass reaches a critical value, approximately given by the M–σ relation (e.g. McConnell & Ma 2013); once this happens, the AGN wind transfers most of its energy to the interstellar medium (ISM), rather than losing it to cooling processes.

In recent years, with the increased availability of outflow data, it became clear that many outflows have mass, momentum, and energy rates that fall below the analytically predicted correlations (e.g. Fiore et al. 2017; Harrison et al. 2018). One interpretation of this phenomenon is that in these galaxies, a large part of the energy carried by the AGN wind does not couple to the ISM (Smith et al. 2019), perhaps due to being efficiently radiated away. In extreme cases, it has been suggested that some outflows might be momentum-conserving rather than energy-conserving (Bischetti et al. 2019; Reeves & Braito 2019; Sirressi et al. 2019). A momentum-conserving outflow has a momentum loading factor $\dot{p}_{\rm out} c / L_{\rm AGN} \sim 1$ and $\dot{E}_{\rm out} / L_{\rm AGN} < 10^{-3}$, consistent with these observations. A possible test of this interpretation is given by the prediction that a rapidly cooling AGN wind would emit a large amount of radiation, $L_{\rm cool} \simeq 0.05 L_{\rm AGN}$ (Bourne & Nayakshin 2013; Nims, Quataert & Faucher-Giguère 2015). This is generally not observed, although in some cases, evidence suggests the presence of cooling wind (Pounds & King 2013). Additionally,

★ E-mail: kastytis.zubovas@ftmc.lt

the lack of detailed information about the distribution of outflowing gas in different phases (molecular, neutral, and ionized), as well as the averaging of mass flow rates over the outflow lifetime, might lead to much lower estimates of momentum flow rates than the simple analytical prediction (Richings & Faucher-Giguère 2018b).

Another explanation of the observed scatter is that the current AGN luminosity is significantly different than the long-term average. The importance of AGN luminosity variations for outflow properties has been hinted at before. King, Zubovas & Power (2011) showed that an outflow might persist for an order of magnitude longer than the AGN episode driving it; this would lead to a substantial population of 'fossil' outflows, some of which have been recently identified (Fluetsch et al. 2019). Zubovas & King (2016) and Zubovas (2019) showed that if the AGN is active sporadically, the outflow behaves at late times as if it was driven by the average AGN luminosity, without much variability due to sudden luminosity changes. Other authors have suggested that AGN luminosity changes might be important in establishing the high observed momentum loading factors (Ishibashi & Fabian 2015), extending the AGN influence throughout the galaxy (Costa et al. 2018) and explaining the variety of observed outflow energy coupling efficiencies (Harrison et al. 2018).

This explanation is attractive because it is based on very robust observational and theoretical results. It is well known that AGNs are variable on all time-scales, and the relativistic winds are similarly variable as well (King & Pounds 2003, 2015). Furthermore, individual AGN episodes last only $\sim 10^5$ yr (King & Pringle 2007; King & Nixon 2015; Schawinski et al. 2015); over this time-scale, even a very rapid outflow with $v_{\rm out} = 1000\,{\rm km\,s^{-1}}$ moves only ~ 100 pc. Any outflows observed further than several hundred parsecs from the AGN are unlikely to have been inflated by the current AGN episode (Nardini & Zubovas 2018; Zubovas 2018). Furthermore, once an AGN episode begins, the outflowing material can only react to it after a time $t_{\rm react} = R_{\rm out}/v_{\rm w} \sim 3 \times 10^4 R_{\rm kpc}$ yr, where $R_{\rm kpc}$ is outflow radius in kiloparsecs. This time-scale is comparable to the lifetime of a single AGN episode, therefore there may be a significant lag between changes in AGN luminosity and changes in outflow properties. More importantly for the interpretation of outflow observations, the currently observed AGN luminosity may be very different even from the luminosity that the outflow is currently reacting to, not to mention the time-averaged energy input rate. The time-averaged rate may correlate with the Eddington luminosity, producing a relation between outflow properties and SMBH mass (González-Alfonso et al. 2017).

In this paper, we investigate the evolution of outflows driven by intermittent AGN episodes, with particular emphasis on the observable correlations between AGN and outflow properties. We show that this model explains the extremely small momentum- and energy-loading factors in PDS 456; we predict that the AGN in this galaxy was active < 10 per cent of the time while the outflow has been expanding. On the other hand, the outflow in Mrk 231 is consistent with continuous driving at the present-day AGN luminosity. The outflow in IRAS F11119+3257 is intermediate between the two, suggesting non-continuous driving, albeit with a large duty cycle. We then consider the expected distribution of momentum- and energy-loading factors for a population of AGN with different duty cycles and compare that with a representative observational sample. We find that the observed and modelled distributions are broadly similar; in particular, up to ~ 15 per cent of outflows are expected to show $\dot{p}_{\rm out} < L_{\rm AGN}/c$, although this fraction depends on both the AGN duty cycle and the host galaxy gas fraction.

We begin the paper by reviewing the salient properties of the wind feedback model, its 1D numerical implementation, and the

AGN luminosity prescription (Section 2). We then present the observational sample of AGN and outflow properties in Section 3. We show results of modelling individual galaxies in Section 4 and the distribution of loading factors in Section 5. We discuss our results in the broader context of AGN outflows in Section 6 and summarize in Section 7.

2 PHYSICAL AND NUMERICAL OUTFLOW MODEL

2.1 Wind outflow model

The AGN wind-driven outflow model was first proposed by King (2003) and later developed mainly in King (2010a) and Zubovas & King (2012). We refer the reader to these papers, as well as to a recent review in King & Pounds (2015), for the details, and only give a brief summary of the salient points of the model.

The energy released by the AGN is communicated to the ISM via wide-angle disc winds (King & Pounds 2003; Nardini et al. 2015). These winds move with quasi-relativistic velocities $v_{\rm w} = \eta c \simeq 0.1c$, where $\eta \simeq 0.1$ is the radiative efficiency of accretion. The kinetic power of the wind is $\dot{E}_{\rm w} \simeq \eta \dot{m} L_{\rm AGN}/2 \simeq 0.05 L_{\rm AGN}$, with $\dot{m} \equiv \dot{M}_{\rm w}/\dot{M}_{\rm acc} \simeq 1$ being the mass-loading factor of the wind compared to the supermassive black hole (SMBH) accretion rate. The wind encounters the ISM, which is relatively stationary ($\sigma_{\rm turb} \ll v_{\rm w}$) and is slowed by a strong shock, which heats the wind material to temperatures of the order of $T_{\rm sh} \sim 10^{11}$ K. The subsequent evolution of the shocked wind depends on whether it cools efficiently. If the wind forms a single-temperature plasma, then cooling is efficient within several hundred parsecs of the nucleus (King 2003) and only the wind momentum is transferred to the ISM. If the momentum is large enough to overcome the weight of the ISM, the gas is pushed away and a large-scale outflow develops; the critical momentum rate, related to the AGN luminosity and hence the SMBH mass, establishes the M–σ relation (King 2003; Murray, Quataert & Thompson 2005). A large-scale outflow might also develop if the shocked wind forms a two-temperature plasma, which cools inefficiently (Faucher-Giguère & Quataert 2012). In either case, the bubble expands adiabatically, can sweep throughout the galaxy spheroid, remove most of the gas there, and quench further star formation (Zubovas & King 2012).

This model explains the basic properties of outflows very well. In particular, it predicts that large-scale massive AGN-driven outflows should have kinetic powers $\dot{E}_{\rm out}$ equal to a few per cent of $L_{\rm AGN}$ and momentum rates $\dot{p}_{\rm out}$ at least an order of magnitude greater than $L_{\rm AGN}/c$, in agreement with observations (Cicone et al. 2014; Fiore et al. 2017; González-Alfonso et al. 2017; Fluetsch et al. 2019; Lutz et al. 2020). However, analytical treatment of the problem is only possible for a few idealized cases, limiting the variety of galaxy properties and AGN luminosity histories that can be explored. One major limitation is that only constant AGN luminosity is tractable analytically. While the outflow is driven, it quickly reaches a quasi-steady state, with constant velocity $v_{\rm out} \sim 1000\,{\rm km\,s^{-1}}$ (in the rest of this paper, we adopt a scaling $v_{1000} \equiv v_{\rm out}/1000\,{\rm km\,s^{-1}}$), mass outflow rate $\dot{M}_{\rm out}$ that can reach more than several hundred $M_\odot\,{\rm yr^{-1}}$ and, consequentially, the momentum and energy loading factors quoted above (King 2005). When the AGN switches off, the outflow coasts for a time up to an order of magnitude longer than the duration of the AGN phase (King et al. 2011).

If the AGN luminosity is allowed to vary significantly over time, one would expect the observed loading factors to vary as well, for two reasons. If the AGN luminosity drops suddenly, the

ionization balance of the gas changes after a delay equal to the light traveltime $t_l = R_{out}/c \sim 3000 R_{kpc}$ yr. The decrease in ionizing flux allows some of the gas to recombine and perhaps cool down to become molecular much faster than if the AGN luminosity had been constant. Therefore, the ionized gas component of the outflow may disappear simply because the gas becomes difficult to detect, rather than because it stops moving. This interpretation is consistent with the observation that outflows in lower luminosity AGN have a higher ratio of molecular-to-ionized mass outflow rates (see fig. 1 in Fiore et al. 2017). A second aspect is the dynamical response of the outflow, which cannot occur much faster than on a dynamical time-scale $t_d \simeq R_{out}/v_{out} \simeq 10^6 R_{kpc} v_{1000}^{-1}$ yr. Naively, one might expect the observed loading factors to increase, at least for a while, as the AGN fades, if this happens on a time-scale shorter than t_d, and decrease as the AGN luminosity increases at the start of a new episode.

2.2 Numerical scheme

Here, we investigate the variations of observed momentum and energy loading factors with a 1D numerical code designed for following the outflow propagation. The code allows for any arbitrary spherically symmetric gravitational potential and matter distribution, as long as the first and second radial derivatives of the enclosed mass, $\partial M(<R)/\partial R$ and $\partial^2 M(<R)/\partial R^2$, can be expressed analytically. The code then integrates the equation of motion for the outflow (for the derivation, see Zubovas & King 2016):

$$\dddot{R} = \frac{\eta L_{AGN}}{MR} - \frac{2\dot{M}\ddot{R}}{M} - \frac{3\dot{M}\dot{R}^2}{MR} - \frac{3\dot{R}\ddot{R}}{R} - \frac{\ddot{M}\dot{R}}{M}$$
$$+ \frac{G}{R^2}\left[\dot{M} + \dot{M}_b + \dot{M}\frac{M_b}{M} - \frac{3}{2}(2M_b + M)\frac{\dot{R}}{R}\right]. \quad (1)$$

Here, M is the mass of gas and M_b is the mass of the background (non-gaseous) matter distribution, including dark matter and stars. The time derivatives of mass are defined as $\dot{M} \equiv \dot{R}\partial M/\partial R$ and $\ddot{M} \equiv \ddot{R}\partial M/\partial R + \dot{R}(\mathrm{d}/\mathrm{d}t)(\partial M/\partial R)$. In all cases, only the relevant mass contained within the current outflow radius R is considered. The first term on the right-hand side of the equation corresponds to the driving of the outflow by the AGN luminosity, the next four terms correspond to the work done by the expanding gas and the increase in outflow mass, and the remaining terms correspond to the work against gravity done while lifting the gas out of the potential well.

Each model galaxy that we investigate is composed of a halo and a bulge. The halo is assumed to have no gas and only contributes to the gravitational potential, while the bulge gas fraction is one of the free parameters of the model. Each model begins with the outflow radius and velocity set to very low values; the precise values are not important, since the outflow evolution is identical after the first few time-steps. The equation of motion (equation 1) is integrated using a simple Eulerian integrator; other, more complicated, integration schemes produce identical results (Zubovas & King 2016).

The parameters we are particularly interested in are defined as follows. The outflow velocity is

$$v_{out} \equiv \dot{R} \equiv \iint \dddot{R}\,\mathrm{d}t\,\mathrm{d}t. \quad (2)$$

The mass outflow rate is defined in a way similar to how it is usually done when analysing observations:

$$\dot{M}_{out} \equiv M_{out}\frac{v_{out}}{R_{out}}, \quad (3)$$

where M_{out} is the total gas mass contained within R_{out}. The momentum loading factor is

$$p_{load} \equiv \frac{\dot{M}_{out}v_{out}c}{L_{AGN}}, \quad (4)$$

and the energy loading factor is

$$E_{load} \equiv \frac{\dot{M}_{out}v_{out}^2}{2L_{AGN}}. \quad (5)$$

In the last two cases, the instantaneous AGN luminosity is used, to mimic the properties of the system that are observationally accessible.

2.3 AGN luminosity variation

In models with varying AGN luminosity, we adopt a temporal evolution prescription based on King & Pringle (2007):

$$L_{AGN} = L_0\left(1 + \frac{t}{t_q}\right)^{-19/16}. \quad (6)$$

This prescription is attractive because it reproduces the observed distribution of AGN Eddington ratios; it has also been shown to be the best for keeping AGN outflow momentum and energy loading factors in the observed range (Zubovas 2018). If the AGN episode initially has $L = L_{Edd}$, its duration, i.e. the time for which $L > 0.01L_{Edd}$, is $t_{ep} = 48t_q$. Together with a recurrence time-scale t_r, this establishes the duty cycle of the AGN, $\delta_{AGN} \equiv t_{ep}/t_r$. In this paper, we consider two values for the duty cycle: a low value $\delta_{AGN} = 0.084$, approximately consistent with observational estimates of the whole galaxy population (Wang, Chen & Zhang 2006); and a five times larger value $\delta_{AGN} = 0.42$, which represents an AGN in a prolonged period of activity, lasting several tens of Myr (Yu & Tremaine 2002; Hopkins et al. 2005), during which high-luminosity states are much more frequent than over the lifetime of the galaxy. In both cases, we use a recurrence time $t_r = 10^6$ yr, while the characteristic time-scales are $t_q = 1750$ yr and $t_q = 8750$ yr, respectively. Our chosen values of t_q correspond to AGN episode durations $t_{ep} = 8.4 \times 10^4$ yr and $t_{ep} = 4.2 \times 10^5$ yr, respectively, consistent with observational (Schawinski et al. 2015) and theoretical (King & Nixon 2015) constraints. We tested that changing both t_q and t_{rep} while keeping their ratio constant has almost no effect on our results, unless t_q becomes so large that the outflow sweeps through the host galaxy in a single episode, but this is unrealistic.

3 OUTFLOW DATA

The AGN sample considered in this work is largely drawn from the recent collections of González-Alfonso et al. (2017), Fluetsch et al. (2019), and Lutz et al. (2020). For many objects, the large-scale outflow is also detected in the neutral and/or ionized phase (e.g. Rupke, Gültekin & Veilleux 2017), with the molecular component that is usually dominant by $\sim$1–2 orders of magnitude over the ionized one (see also Roberts-Borsani 2020).[1] Whenever the cold gas phase is probed in both CO and OH, some discrepancy exists between mass, momentum, and kinetic energy outflow rates based on these two tracers. This difference is mostly due to the smaller (by

---

[1]There is a possible trend towards equi-partition between the molecular and ionized phases at the highest AGN luminosities ($L_{AGN} \gtrsim 10^{47}$ erg s^{-1}; e.g. Fiore et al. 2017), but the typical AGN luminosity in our sample is much lower.

factors of a few) radii inferred from the OH features, while masses and (especially) velocities are in good agreement (see also fig. 6 of Lutz et al. 2020). The origin of this effect is not completely clear, so here we stick to CO-based radii, which are directly measured through imaging data.

Even limited to CO studies, however, there is no accepted convention on the definition of the key outflow properties. For instance, once the association of broad emission lines with the outflow is established (as opposed to a regular velocity field like a rotating disc), the flux is variously integrated over the entire profile or only over its wings, and the outflow velocity can be either identified with the bulk (peak) velocity v_{broad} or with the maximum velocity, $v_{max} = v_{broad} + 2\sigma$, the latter believed to be a proxy of the true (deprojected) gas velocity. Hence, not only the mass (obtained from the flux) but also the dynamical properties, whereby the momentum and energy rates scale as the second and third power of v_{out}, can vary by factors of several simply based on the starting assumptions. Here we therefore give priority to the estimates of Lutz et al. (2020), who revised the literature data with a uniform prescription, for which the outflow velocity is the sum of the net shift of the broad component compared to the systemic velocity and its half-width at a tenth of its peak, and the wings are defined such as the broad component accounts for more than 50 per cent of the total line emission.

When computed as in equation (3), the mass outflow rate corresponds to an isothermal density profile with $R_{out} \gg R_{in}$ (e.g. Rupke, Veilleux & Sanders 2005) and it assumes a constant value in both radius and time. This is clearly an oversimplification, but it represents a convenient and sensible benchmark to make the properties of outflows as obtained in different studies uniform. Several works adopt instead a constant density in the outflow, as this has the advantage that the mass outflow rate does not depend on the exact geometrical structure (i.e. the bi-cone opening angle; e.g. Maiolino et al. 2012; Fiore et al. 2017). This assumption brings a multiplicative factor in the expression above of just 3, yet it is less appropriate for a comparison with our model, also in terms of the implied outflow history (see the discussion in Lutz et al. 2020).

Another major source of uncertainty in the characterization of large-scale outflows resides in the conversion between the observed CO line luminosity (L'_{CO}) and the total molecular mass ($M_{H_2} = M_{out}$), which is usually implemented through the mass-to-light ratio factor α_{CO} (e.g. Bolatto, Wolfire & Leroy 2013a). The typical range of α_{CO} is 0.34–4.3 $M_\odot$ (K km s^{-1} pc^2)$^{-1}$, where the lower limit corresponds to the optically thin case, while the upper limit coincides with the Galactic value.[2] These values are generally derived for the quiescent gas, whose physical conditions are not necessarily representative of the outflow components, for which few constraints are available instead. In some cases, CO emission lines from higher order transitions than $J = 1$–0 are probed. Line luminosity ratios $r_{J_{up}1}$ must then be introduced. However, for low-excitation transitions like $J = 3$–2 and $J = 2$–1 considered here, $r_{J_{up}1} \approx 1$ (e.g. Papadopoulos et al. 2012), hence this can be seen as an additional source of uncertainty on α_{CO} itself. In this work, we adopt $\alpha_{CO} = 0.8$, as per the rotating nuclear discs of ULIRGs (Downes & Solomon 1998), which represent a substantial fraction of the literature samples. Although values as low as $\alpha_{CO} = 0.5$ are used in some works, our choice is still rather conservative if compared, for instance, to $\alpha_{CO} \sim 2.1$, as measured in the outflow of NGC 6240 (Cicone et al. 2018).

In our estimates of the outflowing molecular mass and of the dependent dynamical properties, we account for the scatter of α_{CO}

in individual objects by assuming an uncertainty of 0.3 dex on the total molecular masses of each component. In any case, we expect the choice of a common α_{CO} not to have any global effects on our results, as these will cancel out over a sufficiently large sample. Moreover, while the presence of residual, α_{CO}-related systematics cannot be entirely ruled out, we are confident that these would mostly shift any correlations with the AGN properties by acting on their normalizations, rather than inducing spurious correlations or concealing real ones.

When not explicitly reported, we use uncertainties of 10 and 20 per cent, respectively, on outflow velocities and radial distances. Uncertainties on outflow properties are propagated through Monte Carlo simulations assuming normal or lognormal distributions for the quantities involved. The resulting median and 16th–84th percentiles are assumed as best value and confidence range. Any correction for projection effects is neglected, even for the few objects where tentative geometrical information is available. Finally, we treat the advanced AGN mergers with a close pair of nuclei as single systems, since the luminosity of each AGN cannot be disentangled.

The salient AGN and outflow properties of the 43 objects in our sample are given in Table 1.

4 RESULTS: INDIVIDUAL OBJECTS

Before investigating how well our model reproduces the statistical properties of the whole observational sample, we consider the propagation of outflows in three model galaxies, corresponding to Mrk 231, PDS 456, and IRAS F11119+3257. These objects were chosen for several reasons. First of all, they are all type 1 quasars with disturbed yet compact morphology, likely in the post-coalescence stage, so the spherical symmetry of our models is not too crude an approximation; this would not be the case in, say, the double nuclei of early-stage mergers or Seyfert spiral galaxies. Secondly, all three objects have been reasonably well studied and show evidence of both a small-scale quasi-relativistic wind and one or more large-scale outflows. Finally, these objects help us very clearly illustrate the difference between continuous and intermittent AGN driving.

The salient properties of those galaxies that we used to set up the models are given in Table 2. For each galaxy, we test models with different gas fractions in the bulge, giving $M_g = f_g M_{bulge}$. We assume the bulge density profile to be isothermal and the rest of the mass to be distributed in a halo with an NFW (Navarro, Frenk & White 1997) profile. We also assume that the bulge extends out to the most distant outflow radius, because the gas mass estimates are typically available only at that radius. Therefore, our results should only be considered physical out to the assumed bulge radius; in all subsequent plots, outflow propagation within the bulge is marked with thicker lines than outside it. Within our models, outflow propagation inside the bulge is quite insensitive to the assumed halo density profile, virial mass, and virial radius of each galaxy, as long as $r_{vir} \gg R_{out}$. Each model was integrated until the outflow reached $R_{max} = 25$ kpc, which typically took several tens of Myr. Expansion within the physically constrained bulge region typically takes a few Myr in each model.

Fig. 1 shows the radial profiles of velocity and mass outflow rate in the Mrk 231 model, with the AGN active continuously. The five lines correspond to models with different gas fractions, from gas-poor $f_g = 0.01$ (black solid) to gas-rich $f_g = 0.25$ (orange triple-dot-dashed). We also show the best current observational estimates of outflow properties: CO data from Cicone et al. (2012, triangles) and from Feruglio et al. (2015, histogram, rescaled to $\alpha_{CO} = 0.8$), as well as OH data from González-Alfonso et al. (2017, grey squares). The notable difference between OH and CO data comes mainly from

---

[2]For simplicity, the units of α_{CO} are omitted hereafter.

Table 1. Molecular outflow properties of the sources considered in our analysis.

Source	z	$\log L_{AGN}$ (erg s^{-1})	$\log \dot{M}_{out}$ (M$_\odot$ yr^{-1})	$\log \dot{P}_{out}$ (L_{AGN}/c)	$\log \dot{E}_{out}$ (L_{AGN})	Reference
NGC 253	0.001	42.3	$3.4^{+3.7}_{-1.8}$	$1.2^{+0.4}_{-0.3}$	$-2.8^{+0.4}_{-0.4}$	Bolatto et al. (2013b)
III Zw 35	0.027	42.7	57^{+60}_{-30}	$2.9^{+0.4}_{-0.5}$	$-0.4^{+0.4}_{-0.5}$	Lutz et al. (2020)
PG 0157+001	0.163	45.7	63^{+68}_{-33}	$-0.1^{+0.4}_{-0.3}$	$-3.2^{+0.3}_{-0.4}$	Lutz et al. (2020)
NGC 1068	0.004	45.4	14^{+15}_{-7}	$-1.0^{+0.3}_{-0.4}$	$-4.8^{+0.4}_{-0.4}$	García-Burillo et al. (2014)
NGC 1266	0.007	< 42.2	39^{+42}_{-21}	> 2.8	> -0.5	Lutz et al. (2020)
NGC 1377	0.006	42.2	$6.6^{+7.1}_{-3.5}$	$2.0^{+0.5}_{-0.4}$	$-1.6^{+0.5}_{-0.5}$	Aalto et al. (2012)
NGC 1433	0.004	42.1	$0.9^{+1.1}_{-0.5}$	$1.2^{+0.4}_{-0.4}$	$-2.6^{+0.5}_{-0.5}$	Combes et al. (2013)
NGC 1614	0.016	44.0	19^{+20}_{-10}	$1.1^{+0.4}_{-0.3}$	$-2.1^{+0.4}_{-0.4}$	García-Burillo et al. (2015)
NGC 1808	0.003	42.8	$3.4^{+3.6}_{-1.7}$	$1.0^{+0.5}_{-0.5}$	$-2.8^{+0.6}_{-0.5}$	Salak et al. (2016)
IRAS 05083+7936	0.054	44.2	79^{+86}_{-42}	$1.9^{+0.4}_{-0.4}$	$-1.0^{+0.5}_{-0.4}$	Lutz et al. (2020)
IRAS 05189−2524	0.043	45.6	37^{+39}_{-19}	$-0.1^{+0.3}_{-0.4}$	$-3.3^{+0.4}_{-0.3}$	Lutz et al. (2020)
NGC 2146	0.003	42.9	10^{+10}_{-6}	$1.7^{+0.3}_{-0.4}$	$-1.8^{+0.4}_{-0.4}$	Tsai et al. (2009)
NGC 2623 (a)	0.019	44.2	11^{+13}_{-6}	$0.9^{+0.3}_{-0.3}$	$-2.1^{+0.3}_{-0.4}$	Lutz et al. (2020)
NGC 2623 (b)			$0.4^{+0.4}_{-0.2}$	$-0.8^{+0.4}_{-0.3}$	$-4.0^{+0.4}_{-0.3}$	Lutz et al. (2020)
IRAS 08572+3915	0.058	45.7	345^{+376}_{-176}	$1.1^{+0.3}_{-0.3}$	$-1.8^{+0.5}_{-0.7}$	Cicone et al. (2014)
IRAS 09111−1007W	0.054	< 43.5	64^{+70}_{-33}	> 2.0	> -1.3	Lutz et al. (2020)
M 82	0.001	41.5	$6.7^{+7.0}_{-3.5}$	$2.6^{+0.4}_{-0.4}$	$-1.2^{+0.4}_{-0.4}$	Walter, Weiss & Scoville (2002)
NGC 3256	0.009	44.0	50^{+39}_{-22}	$1.8^{+0.3}_{-0.3}$	$-1.2^{+0.3}_{-0.3}$	Sakamoto et al. (2014)
IRAS 10565+2448	0.043	44.8	95^{+99}_{-49}	$1.1^{+0.5}_{-0.4}$	$-2.0^{+0.5}_{-0.5}$	Cicone et al. (2014)
IRAS 11119+3257 (a)	0.189	46.0	203^{+222}_{-108}	$0.6^{+0.4}_{-0.4}$	$-2.2^{+0.5}_{-0.5}$	Tombesi et al. (2015)
IRAS 11119+3257 (b)	–	–	81^{+92}_{-42}	$0.2^{+0.4}_{-0.4}$	$-2.6^{+0.5}_{-0.5}$	Veilleux et al. (2017)
NGC 3628	0.003	41.6	$1.3^{+1.4}_{-0.7}$	$1.8^{+0.6}_{-0.5}$	$-2.0^{+0.5}_{-0.5}$	Tsai et al. (2012)
ESO 320–G030	0.011	41.8	10^{+3}_{-1}	$3.0^{+1.1}_{-0.4}$	$-0.3^{+1.1}_{-0.4}$	Pereira-Santaella et al. (2016)
IRAS 12112+0305	0.073	44.8	198^{+198}_{-96}	$1.4^{+0.7}_{-0.4}$	$-1.7^{+0.7}_{-0.4}$	Pereira-Santaella et al. (2018)
IRAS 12224−0624	0.026	41.7	23^{+24}_{-12}	$3.6^{+0.5}_{-0.5}$	$0.6^{+0.5}_{-0.5}$	Lutz et al. (2020)
NGC 4418	0.007	44.4	$9.1^{+9.5}_{-4.6}$	$0.3^{+0.6}_{-0.5}$	$-2.9^{+0.5}_{-0.6}$	Lutz et al. (2020)
Mrk 231	0.042	46.0	330^{+375}_{-169}	$0.7^{+0.4}_{-0.4}$	$-2.2^{+0.4}_{-0.4}$	Cicone et al. (2012)
IRAS 13120−5453	0.031	43.8	134^{+147}_{-68}	$2.1^{+0.4}_{-0.4}$	$-1.2^{+0.4}_{-0.4}$	Lutz et al. (2020)
M 51	0.002	43.2	$1.9^{+2.1}_{-1.0}$	$0.3^{+0.5}_{-0.4}$	$-3.4^{+0.5}_{-0.6}$	Querejeta et al. (2016)
Mrk 273	0.038	45.5	190^{+197}_{-97}	$1.1^{+0.5}_{-0.4}$	$-2.1^{+0.4}_{-0.4}$	Cicone et al. (2014)
4C +12.50	0.122	45.6	128^{+140}_{-65}	$0.6^{+0.4}_{-0.4}$	$-1.8^{+0.4}_{-0.4}$	Dasyra & Combes (2011)
J135646.10+102609.0	0.123	45.7	109^{+119}_{-56}	$0.3^{+0.5}_{-0.4}$	$-2.7^{+0.4}_{-0.4}$	Sun et al. (2014)
Circinus Galaxy	0.001	43.4	$1.3^{+1.4}_{-0.7}$	$0.1^{+0.4}_{-0.3}$	$-3.5^{+0.4}_{-0.3}$	Zschaechner et al. (2016)
IRAS 14348−1447	0.083	45.1	199^{+154}_{-85}	$1.1^{+0.5}_{-0.4}$	$-2.1^{+0.6}_{-0.4}$	Pereira-Santaella et al. (2018)
IRAS 14378−3651	0.068	< 44.0	208^{+153}_{-88}	> 2.0	> -1.0	González-Alfonso et al. (2017)
Arp 220	0.018	45.0	52^{+43}_{-22}	$0.7^{+0.6}_{-0.3}$	$-2.4^{+0.5}_{-0.4}$	Barcos-Muñoz et al. (2018)
Mrk 876	0.129	45.8	738^{+769}_{-377}	$1.4^{+0.3}_{-0.3}$	$-1.4^{+0.3}_{-0.4}$	Lutz et al. (2020)
NGC 6240	0.024	44.9	262^{+298}_{-140}	$1.4^{+0.4}_{-0.4}$	$-1.8^{+0.5}_{-0.5}$	Feruglio et al. (2013)
IRAS 17020+4544	0.060	45.1	322^{+336}_{-164}	$1.9^{+0.5}_{-0.5}$	$-0.7^{+0.5}_{-0.4}$	Lutz et al. (2020)
IRAS 17208−0014	0.043	45.0	112^{+121}_{-56}	$1.4^{+0.9}_{-0.4}$	$-1.3^{+0.8}_{-0.5}$	Lutz et al. (2020)
PDS 456 (a)	0.184	47.1	91^{+74}_{-40}	$-1.0^{+0.4}_{-0.3}$	$-3.9^{+0.5}_{-0.3}$	Bischetti et al. (2019)
PDS 456 (b)			21^{+11}_{-6}	$-1.6^{+0.4}_{-0.3}$	$-4.5^{+0.4}_{-0.3}$	Bischetti et al. (2019)
NGC 6764	0.008	42.7	$0.02^{+0.02}_{-0.01}$	$-1.7^{+0.4}_{-0.4}$	$-6.1^{+0.4}_{-0.4}$	Leon et al. (2007)
IRAS 20100−4156	0.130	45.5	689^{+751}_{-359}	$1.6^{+0.3}_{-0.3}$	$-1.3^{+0.4}_{-0.3}$	Gowardhan et al. (2018)
IC 5063	0.011	44.6	13^{+13}_{-7}	$0.3^{+0.3}_{-0.3}$	$-3.0^{+0.3}_{-0.3}$	Morganti et al. (2013)
IRAS 20551−4250	0.043	45.1	67^{+74}_{-35}	$0.7^{+0.4}_{-0.3}$	$-2.3^{+0.3}_{-0.4}$	Lutz et al. (2020)
IRAS 22491−1808	0.078	44.9	91^{+94}_{-47}	$0.8^{+0.4}_{-0.4}$	$-2.5^{+0.4}_{-0.3}$	Pereira-Santaella et al. (2018)
IRAS 23060+0505	0.173	45.9	361^{+362}_{-180}	$0.6^{+0.3}_{-0.3}$	$-2.4^{+0.3}_{-0.3}$	Lutz et al. (2020)
IRAS 23365+3604	0.064	44.6	51^{+54}_{-27}	$1.1^{+0.4}_{-0.4}$	$-2.1^{+0.5}_{-0.4}$	Cicone et al. (2014)

Notes. Source redshifts were retrieved from the NASA/IPAC Extragalactic Database, http://ned.ipac.caltech.edu/. AGN luminosities are based on different multiwavelength indicators (such as IR colours and [O IV] 25.9, 6 μm, 5100 Å, [O III] 5007 Å, 1350 Å, and 2–10 keV luminosities]), and have uncertainties of 0.1–0.4 dex. Outflow properties were adapted from the original references as described in Section 3. For sources with spatially distinct components, (a) is close to the nucleus and (b) is farther out.

Table 2. Parameters of the Mrk 231, PDS 456, IRAS F11119+3257, and 'generic Seyfert' galaxy models. Virial masses and radii are estimated from rotational velocities. Bulge radii are set equal to the radius within which gas mass estimates are provided in the literature, and bulge masses are calculated from observationally determined velocity dispersions. SMBH masses were obtained from the $H\beta$ line width and the de-reddened 5100 Å luminosity, applying the radius–luminosity relation of Bentz et al. (2013) with a virial factor of 4.3. The data were retrieved from Zheng et al. (2002) for Mrk 231 and IRAS F11119, and from Torres et al. (1997) and Simpson et al. (1999) for PDS 456. AGN luminosities were obtained from the different IR diagnostics of Veilleux et al. (2009) for Mrk 231 and IRAS F11119, and from the de-reddened 1350 Å flux (Hamann et al. 2018) with bolometric correction by Richards et al. (2006) for PDS 456.

Parameter	Mrk 231	PDS 456	IRAS F11119 + 3257	Seyfert
Virial mass (M_{vir})	$1.18 \times 10^{13} \, M_\odot$	$1.26 \times 10^{12} \, M_\odot$	$10^{15} \, M_\odot$	$2 \times 10^{11} \, M_\odot$
Virial radius (r_{vir})	662 kpc	235 kpc	2905 kpc	180.5 kpc
Concentration (c)	10	10	10	10
Bulge radius (r_{bulge})	2 kpc	5 kpc	15 kpc	2 kpc
Bulge mass (M_{bulge})	$5.4 \times 10^{10} \, M_\odot$	$3.8 \times 10^{10} \, M_\odot$	$10^{11} \, M_\odot$	$8 \times 10^9 \, M_\odot$
SMBH mass (M_{SMBH})	$1.8 \times 10^8 \, M_\odot$	$1.4 \times 10^9 \, M_\odot$	$1.0 \times 10^8 \, M_\odot$	$5 \times 10^6 \, M_\odot$
AGN luminosity (Eddington ratio):				
Continuous ($L_{AGN, c}(f_c)$)	$9.0 \times 10^{45} \, erg \, s^{-1}$ (0.4)	$1.2 \times 10^{47} \, erg \, s^{-1}$ (0.7)	$1.1 \times 10^{46} \, erg \, s^{-1}$ (0.9)	n/a
Initial ($L_{0, r}(f_{0, r})$)	n/a	$1.7 \times 10^{47} \, erg \, s^{-1}$ (1)	$2.9 \times 10^{46} \, erg \, s^{-1}$ (2.3)	$3.3 \times 10^{44} \, erg \, s^{-1}$ (0.5)
Duty cycle (δ_{AGN})	n/a	0.084	0.42	0.084
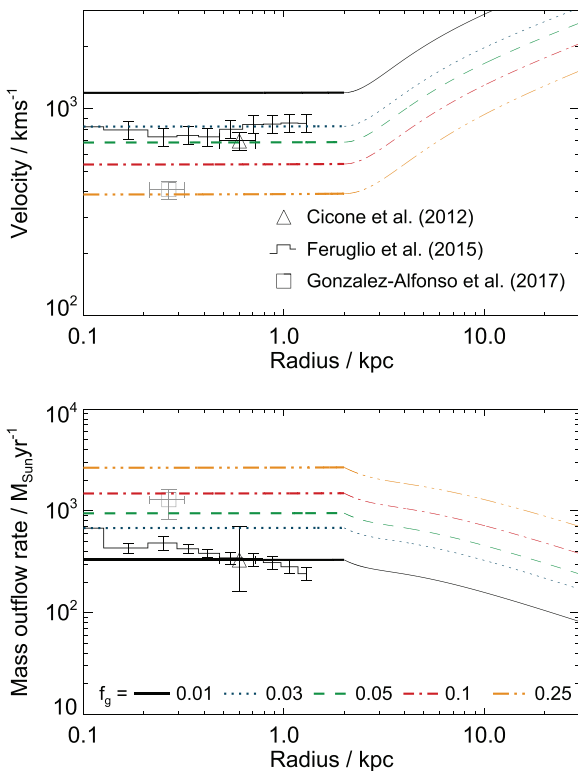
Figure 1. Outflow evolution in Mrk 231 with a continuous AGN energy injection, for models with different gas fractions. Observed outflow properties marked with triangles (CO Cicone et al. 2012), histograms (CO Feruglio et al. 2015), and squares (OH González-Alfonso et al. 2017).

differences in radius estimates (see Section 3), and we generally consider the more conservative CO data in the following discussion. Note, however, that it is possible that OH data traces a denser, and hence slower, outflow in this object.

The almost constant outflow velocity with radius derived by Feruglio et al. (2015), which agrees with the earlier result (Cicone et al. 2012), is well explained by our model, assuming a rather low gas fraction ($0.02 < f_g < 0.05$). The inferred molecular gas content ($M_{H_2} \simeq 5 \times 10^9 M_\odot$; Cicone et al. 2012) corresponds to a

gas fraction $f_g \sim 0.09$, somewhat higher than our preferred values. However, the mass estimate depends sensitively on the assumed conversion factor of CO to H_2, with an uncertainty of at least a factor of two, which brings our model in line with the observational estimate. The mass outflow rate predicted by our models is marginally higher than observed: $\dot{M}_{model} \sim 500$–$1000 M_\odot \, yr^{-1}$, compared with $\dot{M}_{obs} \sim 150$–$700 M_\odot \, yr^{-1}$. However, one should keep in mind that our models assume perfectly spherically symmetric outflows; if the outflow only encompasses a solid angle of 2π as seen from the nucleus, the expected mass outflow rate drops by a factor two and comes well in line with observational estimates. We also note that Feruglio et al. (2015) find the mass outflow rate decreasing slightly with radius, a result which our models do not replicate. Two possible solutions to the discrepancy are a different gas density distribution (however, this would result in the outflow velocity increasing with radius) and/or the outflow solid angle decreasing with radius. This latter possibility seems rather natural if some of the outflowing material slows down and never makes it out of the galaxy, as recently suggested by Fluetsch et al. (2019).

The momentum- and energy-loading factors of the modelled outflows fall in the range $8 < p_{load} < 20$ and $0.012 < E_{load} < 0.015$, close to the observationally derived values $p_{load, obs} \simeq 5$ and $E_{load, obs} \sim 0.006$ (Cicone et al. 2012; Feruglio et al. 2015). The outflow in Mrk 231 also has a substantial neutral component (Rupke & Veilleux 2011; Rupke et al. 2017), so the total momentum and energy loading factors are consistent with model predictions. In addition, the outflow might be non-spherical and some of its material might slow down as it moves away from the nucleus (see preceding paragraph); these two effects would result in lower loading factors than in the idealized case.
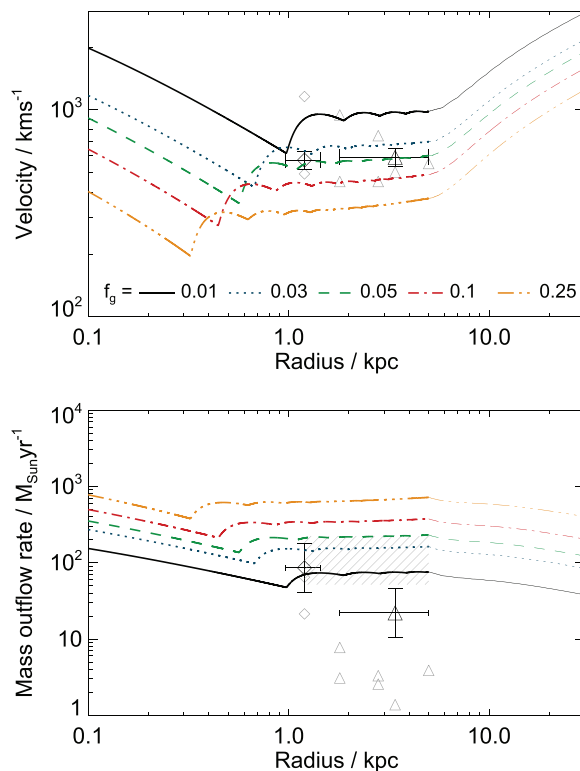
Outflow propagation in PDS 456 shows a marked contrast with the Mrk 231 model. In Fig. 2 we show the properties of an outflow in this system driven by a constant-luminosity AGN. The triangle and diamond data points correspond to the 'extended' and 'central' outflow components identified by Bischetti et al. (2019), with grey points showing smaller subcomponents and the shaded region in the bottom plot showing the total mass outflow rate. We show a 20 per cent radius error for the central component, while all other errors are as given by Bischetti et al. (2019), with appropriate rescalings (a constant density was assumed in the original analysis for the central outflow). The very low observed values of momentum and
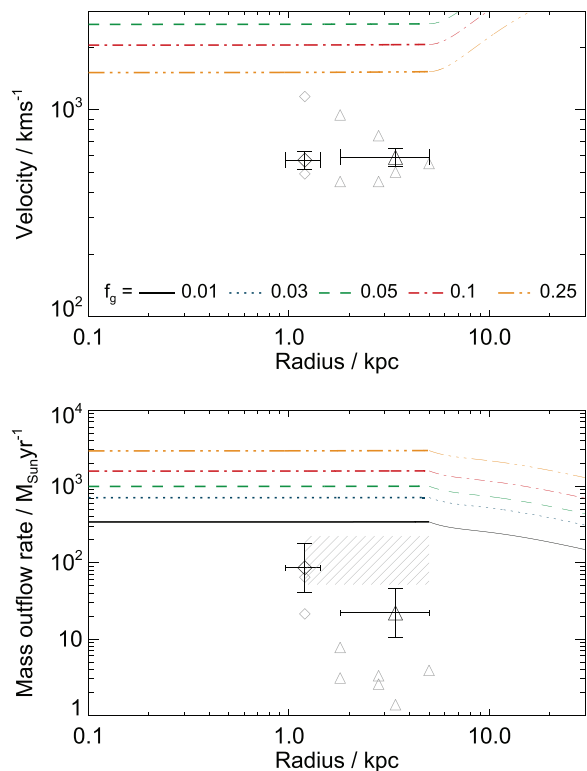
Figure 2. Same as Fig. 1, but for the model of PDS 456. Points show observational data (Bischetti et al. 2019): diamond represents the central component, triangle corresponds to the extended outflow. Fainter points show sub-components. The shaded region in the bottom plot represents the sum of mass outflow rates of both central an extended components.

Figure 3. Same as Fig. 2, but for a varying AGN luminosity history with $\delta_{AGN} = 0.084$.

energy loading factors led these authors to suggest that the outflow in PDS 456 might be driven by the AGN momentum, rather than energy input. Our model results also clearly show that an outflow driven by the energy of a continuous AGN episode has properties inconsistent with the observed data: the model outflow is either much faster than the observed one, or carries much more mass, or both. One way of reconciling these results with observations is by assuming that the molecular gas comprises only a small fraction of the total outflow. However, in order to get the right outflow velocity, the fraction of the bulge mass participating in the outflow should be $f_g > 0.25$, i.e. $M_{gas} (< 5\text{kpc}) > 9.5 \times 10^9 \, M_\odot$, which is at least a factor of 40 greater than the observed outflowing molecular gas mass (Bischetti et al. 2019). In general, when molecular gas is observed, it tends to dominate the mass budget of the outflow (see Section 3). Therefore we are confident that the observed molecular outflow comprises a significant, and most probably dominant, part of the total outflow.

Another way to reconcile observations and model results is to consider a non-continuous AGN luminosity history. Fig. 3 shows the results of such a simulation, where we adopt the luminosity history as described in Section 2.3 with a duty cycle $\delta_{AGN} = 0.084$. Both outflow velocities and mass flow rates decrease significantly compared to the continuous-AGN model, and agree quite well with observed data, assuming $0.03 < f_g < 0.05$. After a few AGN episodes, the variation of AGN luminosity no longer has a noticeable effect on the outflow velocity. This means that the values of momentum and energy loading factors vary significantly with each AGN episode, being inversely proportional to L_{AGN} (see also Zubovas 2018). There are periods of time when the AGN can be observed at its present-

day luminosity $L_{AGN} = 1.2 \times 10^{47} \, \text{erg s}^{-1}$ simultaneously with the observed outflow properties. The momentum and energy loading factors at those times are $\dot{p}_{out} < L_{AGN}/c$ and $\dot{E}_{out} < 10^{-3} L_{AGN}$, again consistent with observations (Bischetti et al. 2019).

An AGN luminosity history consisting of multiple episodes might also explain the presence of spatially distinct outflow components in this galaxy. The extended outflow may have been inflated by an earlier series of AGN episodes, while the central one has been launched more recently, collecting the gas that had been too dense to be removed by the first outflow. Separate subcomponents of the outflows may emerge due to different gas densities in different directions, which lead to some parts of the outflow moving faster than others. However, this is a very tentative interpretation; we consider it in more detail in the Discussion (Section 6.4).

The situation in IRAS F11119+3257 is intermediate between the two previous cases. Figs 4 and 5 show the expansion of the outflow in this galaxy for continuous and intermittent driving, respectively, with data points from Tombesi et al. (2015, squares) and Veilleux et al. (2017, diamonds). Once again, continuous driving is unable to reproduce both the velocity and mass outflow rate of the observed large-scale outflow, although the discrepancy is not as large as in the case of PDS 456. Meanwhile, the inner outflow at $R = 300 \, \text{pc}$ can be explained by the model, assuming that $0.05 < f_g < 0.1$ and that the outflow does not cover the whole sky when looking from the AGN position. On the other hand, intermittent driving, with a high duty cycle $\delta_{AGN} = 0.42$, produces reasonable agreement for the outer outflow, assuming a rather low gas fraction of $f_g = 0.01$. This gas fraction corresponds to $M_g = 10^9 \, M_\odot$ within $R = 15 \, \text{kpc}$, as observed (Veilleux et al. 2017). The inner outflow is much younger (its approximate flow time-scale is $t_{fl} \sim 4 \times 10^5 \, \text{yr}$, while the outer outflow has $t_{fl} \sim 7 \times 10^6 \, \text{yr}$, cf. Veilleux et al. 2017) and may be
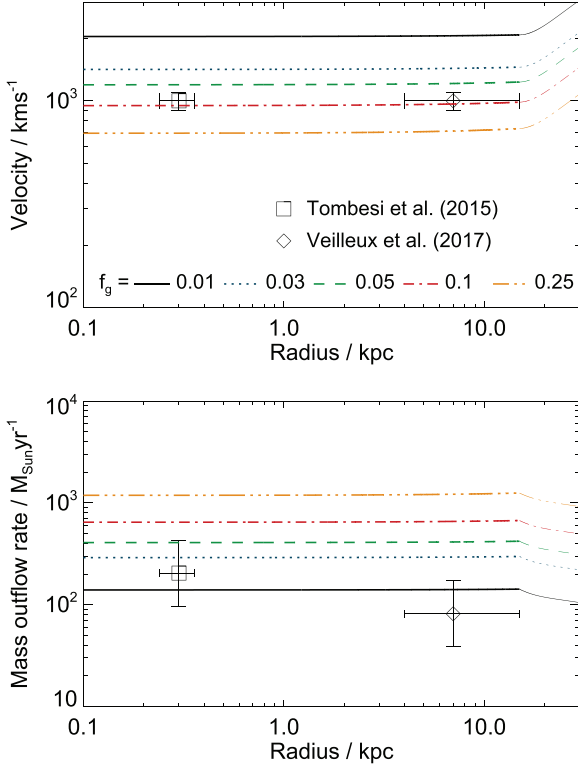
Figure 4. Same as Fig. 1, but for the model of IRAS F11119+3257. Points represent outflow data from Tombesi et al. (2015, squares) and Veilleux et al. (2017, diamonds).
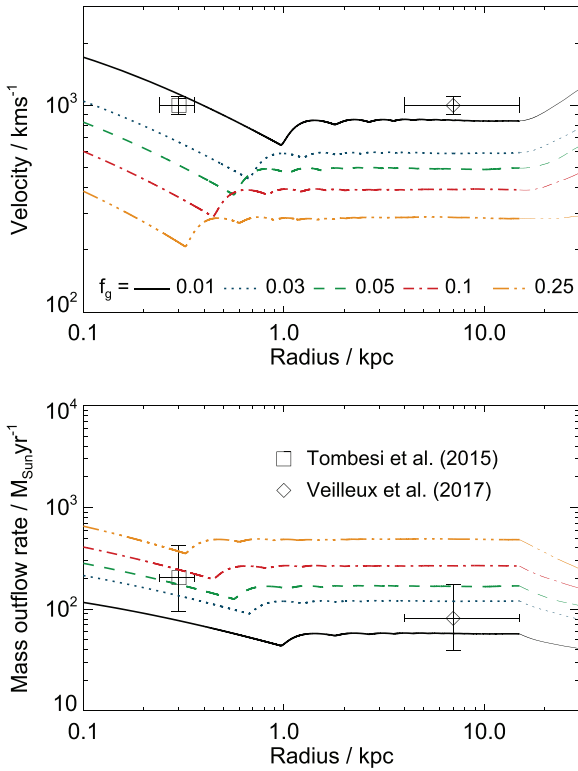
Figure 5. Same as Fig. 4, but for a varying AGN luminosity history with $\delta_{\mathrm{AGN}} = 0.42$.

driven by the current AGN episode, while the outer one is likely to be the product of numerous older episodes.

The difference between outflow parameters in continuous and intermittent AGN luminosity simulations is easy to understand qualitatively. Once the outflow expands beyond the central few hundred parsecs, its behaviour gradually begins to follow the time-averaged energy input from the AGN, rather than the instantaneous luminosity. If the AGN is strongly variable, the time-averaged input is significantly smaller than it would be if the AGN was radiating continuously at $L = L_{\mathrm{max}}$ or close to it. In fact, with the luminosity prescription we choose, the total energy emitted by the AGN from the beginning of an episode to the time its luminosity drops below $0.01 L_{\mathrm{Edd}}$ is

$$E_{\mathrm{out,r}} \simeq 2.75 t_{\mathrm{q}} L_{\mathrm{max}} \simeq 0.057 t_{\mathrm{r}} \delta_{\mathrm{AGN}} L_{\mathrm{max}}. \qquad (7)$$

Note that we assumed $t_{\mathrm{r}} > t_{\mathrm{ep}}$ when calculating the above expression. A constant-luminosity AGN episode emits

$$E_{\mathrm{out,c}} = t_{\mathrm{r}} L_{\mathrm{max}} \qquad (8)$$

over a time t_{r}. Therefore, an outflow driven by an intermittent AGN eventually behaves similarly to how it would if it were driven by a continuous energy injection at a fraction $0.057 \delta_{\mathrm{AGN}}$ of the maximum rate. With the two values of duty cycle that we use, this corresponds to an energy input of 0.004 and 0.024 of the maximum rate. The outflow energy rate would then comprise the same fraction of the continuously driven outflow energy rate, and the momentum rate would be a fraction $(E_{\mathrm{out,r}}/E_{\mathrm{out,c}})^{2/3}$ of the continuously driven one. If the current L_{AGN} is higher than its long-term average $0.057 \delta_{\mathrm{AGN}} L_{\mathrm{max}}$, the derived momentum and energy loading factors will be correspondingly lower than expected from analytical calculations. Conversely, if the AGN has recently faded and its current luminosity is much lower than the average, the observed outflow would appear abnormally powerful.

5 RESULTS: LOADING FACTOR DISTRIBUTION

Individual object observations effectively represent only snapshots of the co-evolution of the AGN and its outflow. It is difficult to know which observations represent 'typical' cases for outflows or even if such 'typical' cases exist. However, by considering what values of momentum and energy loading factors would be observed at random times in our simulations, we can better understand how likely the observed low loading factors are.

In order to produce a set of simulation results encompassing a greater variety of possible galaxy properties than those of Mrk 231, PDS 456, and IRAS F11119, we run simulations with two vastly different sets of galaxy properties. One set of properties is the same as those of PDS 456, while the other corresponds to a smaller galaxy with a much weaker Seyfert AGN (see the rightmost column in Table 2). Such an AGN has a 500 times lower luminosity than PDS 456 and produces outflows with velocities $100\,\mathrm{km\,s^{-1}} < v_{\mathrm{out}} < 300\,\mathrm{km\,s^{-1}}$ and mass flow rates $5\,\mathrm{M_{\odot}\,yr^{-1}} < \dot{M}_{\mathrm{out}} < 40\,\mathrm{M_{\odot}\,yr^{-1}}$. However, the momentum and energy loading factor distributions are virtually indistinguishable between the Seyfert and PDS 456 models, provided that we choose the same threshold, in terms of Eddington ratio, for the selection of AGN (see below). Therefore, we only present the results of PDS 456 models. We also explore the effect of gas density by running simulations with gas fractions ranging from a relatively gas-poor $f_{\mathrm{g}} = 0.05$ to an extremely gas-rich $f_{\mathrm{g}} = 0.8$. We show the results of the two extreme cases; other cases produce loading factor distributions intermediate between these ones.
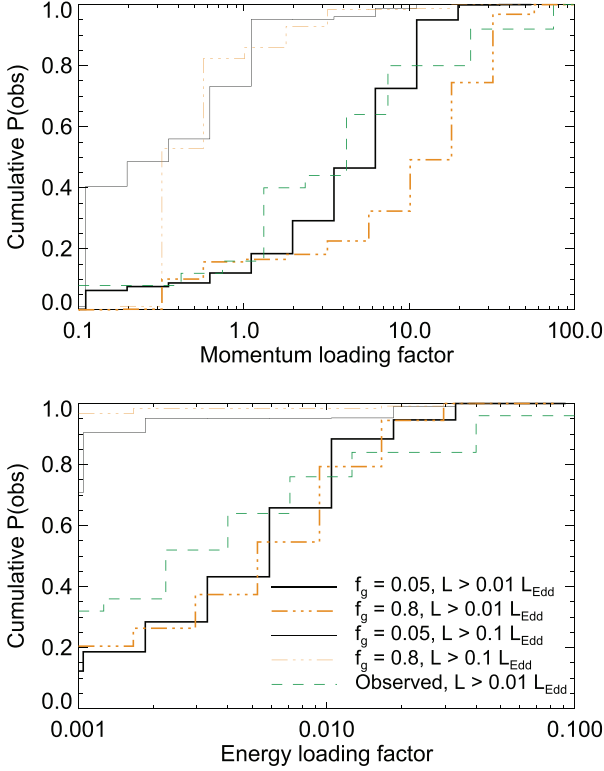
Figure 6. Cumulative distribution of observable instantaneous momentum (top) and energy (bottom) loading factors in quasar (PDS 456) models with different gas fractions (black solid line for $f_g = 0.05$, orange dash-triple-dotted line for $f_g = 0.8$) and different AGN selection thresholds (thin lines for $L_{AGN} > 0.1L_{Edd}$, thick lines for $L_{AGN} > 0.01L_{Edd}$). This includes only outflows with $R_{out} < 10$ kpc. The green dashed line shows loading factor distribution of observed molecular outflows in AGN with $L_{AGN} > 0.01L_{Edd}$.

The loading factors that can be observed depend strongly on the threshold for detection and/or selection of AGN. Although realistic observational thresholds are based on luminosity (either bolometric or, more frequently, of a given indicator), physically, the Eddington ratio f_{Edd} is more important. Here, we present results using two selection thresholds: $L > 0.1L_{Edd}$ and $L > 0.01L_{Edd}$, where $L_{Edd} = 1.7 \times 10^{47}$ erg s^{-1} for the PDS 456 models. The lower threshold corresponds approximately to the canonical switch of accretion mode from hot and spherical to a thin disc (Best & Heckman 2012; Sądowski et al. 2013). The higher threshold leads to only the brightest AGN being selected; this may represent a situation where only a sample of the very brightest AGN is selected by luminosity, since such galaxies must have both high SMBH masses and high f_{Edd}. In addition, in all models, we only consider outflows within 10 kpc of the nucleus, as it is unlikely the AGN would be able to continue flickering on a $\sim 10^4$ yr time-scale once most of the gas is removed well beyond the bulge (Zubovas, Bourne & Nayakshin 2016).

Fig. 6 shows the expected cumulative distributions of momentum (top) and energy (bottom) loading factors that could be observed at random times. The different line colours correspond to models with the lowest ($f_g = 0.05$, black solid) and highest ($f_g = 0.8$, orange triple-dot-dashed) gas fractions. Line thicknesses correspond to different selection thresholds: $L > 0.01L_{Edd}$ (thick lines, lower probabilities) and $L > 0.1L_{Edd}$ (thin lines, higher probabilities).

Looking at the AGN with $L > 0.01L_{Edd}$, we see that galaxies with higher gas fractions tend to have higher average momentum

loading factors, therefore the probability of observing low loading factors is lower in these models; the energy loading factors show no dependence on gas fraction. It is very likely that a randomly chosen system would show a momentum loading factor smaller than the analytical prediction $\dot{p} \simeq 20L_{AGN}/c$: in the lowest density model, this probability is $P \sim 95$ per cent, and even in the highest density model, it is still $P \sim 60$ per cent. The probability of detecting outflows with $\dot{p} < L_{AGN}/c$ is small but non-negligible, ~ 10–15 per cent depending on gas density. The instantaneous energy loading factors are almost uniformly distributed up to $E_{load} \simeq 0.015$, also suggesting that observed values of $\dot{E} < 0.01L_{AGN}$ should be common ($P \sim 70$ per cent). The dearth of energy loading factors > 0.02 is expected, because even with continuous driving, the kinetic energy of the outflow is expected to be only $\sim 1/3$ of the total energy transferred from the AGN (Zubovas & King 2012), i.e. $\sim \eta/6 \sim 0.016$; the rest of the wind energy is used up to do work against gravity and $p dV$ work.

If we concentrate only on the brightest AGN, using a detection threshold $L > 0.1L_{Edd}$ (thin lines in the figure), the expected momentum and energy loading factor distributions become much more extreme. The instantaneous momentum loading factor essentially never rises above 4, even for the highest density models, and the probability of observing $\dot{p} < L_{AGN}/c$ is as high as 70–80 per cent, almost independent of gas density. Energy loading factors are essentially always below 0.001. The ~ 5 per cent of cases with higher energy loading factors correspond to the first AGN episode, when the outflow is very close to the nucleus.

For comparison, we plot the momentum and energy loading factor distribution of observed molecular outflows with $L_{AGN} > 0.01L_{Edd}$ as green dashed histograms. The momentum loading factor distribution mostly follows the low-f_g model, as might be expected for local, generally gas-poor, galaxies. Some of the higher momentum loading factors might be the result of higher gas fractions. The observed energy loading factor distribution is broader, with ~ 20 per cent of observed outflows having $E_{load} > 0.02$. As we show in the next subsection, this difference may be the result of real AGN having a variety of duty cycles.

5.1 Effect of AGN duty cycle

In Fig. 7, we show the same result as in Fig. 6, but for models with a five times higher duty cycle $\delta_{AGN} = 0.42$. In this case, all loading factor distributions are significantly broader, with the median momentum loading factor being $\dot{p} \sim 14L_{AGN}/c$ for $f_g = 0.05$ and $\dot{p} \sim 30L_{AGN}/c$ for $f_g = 0.8$. Meanwhile, energy loading factors tend to stay rather small, with the median $\dot{E}_{out,med} \simeq 0.02L_{AGN}$, although occasionally the effective outflow energy rate rises as high as $\dot{E}_{out} \sim 0.06L_{AGN}$. The probability of observing $\dot{p}_{out} < L_{AGN}/c$ is 2–6 per cent. If only the brightest AGN are selected (thin lines), the typical loading factors decrease, in a similar fashion to the low-duty-cycle model, and the probability of observing $\dot{p}_{out} < L_{AGN}/c$ rises to 20–35 per cent.

The differences between the loading factor distributions in the low- and high-duty-cycle models arise from the average outflow energy. The AGN energy input is five times higher in the high-δ_{AGN} model, therefore the outflow energy (momentum) rate is also 5 ($5^{2/3} \sim 3$) times higher. The distribution of AGN luminosities, on the other hand, does not change between the two models, since the duty cycle only affects the duration of the quiescent period between episodes, which is not included when selecting the AGN for these mock observations. As a result, the average momentum (energy) loading factor that has the same cumulative probability is ~ 3 (~ 5)
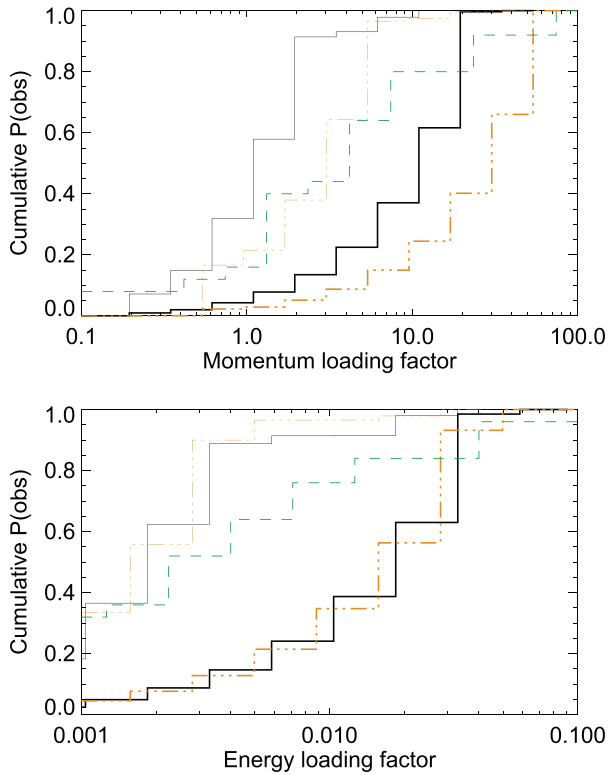
Figure 7. Same as Fig. 6, but with a five times longer AGN episode duration (five times higher duty cycle).

times higher in the high-duty-cycle model than in the low-duty-cycle one, as seen in Figs 6 and 7. During the quiescent phase, the outflow slows down more in the low-duty-cycle model, therefore once a new AGN episode begins, the instantaneous momentum and energy loading factors are much lower.

The distribution of observed loading factors (green dashed histograms) is broadly consistent with the models. The agreement is better when the loading factors are higher; conversely, the low-duty-cycle models fit the data better at the low-loading-factor end. This behaviour is qualitatively understandable: AGN with high duty cycles have more powerful outflows and therefore tend to show higher loading factors, so a mix of AGN with different duty cycles should show a distribution that matches both low- and high-duty cycle models at different parts of the distribution.

6 DISCUSSION

6.1 Correlation between outflows and UFOs

Wide-angle disc winds (see Section 2) have been observed in many AGN; they are typically called ultrafast outflows, or UFOs (Tombesi et al. 2010a,b, 2012; Gofford et al. 2013). In Mrk 231 (Feruglio et al. 2015), PDS 456 (Reeves, O'Brien & Ward 2003; Bischetti et al. 2019) and IRAS F11119+3257 (Tombesi et al. 2015; Veilleux et al. 2017), both wind and outflow have been observed simultaneously. In general, UFO properties correlate with those of the AGN much better than with the outflow. This is to be expected: the UFO is detected at distances $r_{UFO} \ll 1$ pc from the nucleus and can react to changes in AGN luminosity on time-scales of a few months or shorter (Matzeu et al. 2017). In fact, most UFOs might have ages of several weeks or months (King & Pounds 2015).

The observed UFO kinetic power is very similar to that of the outflow in Mrk 231 (Feruglio et al. 2015), although this is not the case in IRAS F11119+3257 and PDS 456 (Veilleux et al. 2017; Nardini & Zubovas 2018; Bischetti et al. 2019). This situation echoes the correlations between outflow properties and AGN luminosity. Therefore, we feel confident in using AGN luminosity as an effective tracer of wind power transferred to the outflow.

In our models, we assume a constant 5 per cent efficiency of energy transfer from the AGN to the wind and, subsequently, to the outflow. Real UFOs show a spread of kinetic powers that range from $10^{-3}L_{AGN}$ to $>0.1L_{AGN}$ (Tombesi et al. 2013; Fiore et al. 2017). This spread may be the result of different SMBH spins, which lead to different radiative efficiencies (King & Pounds 2015), rapid UFO variability in time (Pounds et al. 2016; Reeves, Lobban & Pounds 2018a; Reeves et al. 2018b), clumps of different density moving into and out of the line of sight (Matzeu et al. 2016; Reeves et al. 2020), different viewing angles (Matthews et al. 2016; Giustini & Proga 2019), or other differences in the details of wind geometries. Launching mechanisms are very important as well: at high Eddington ratios, continuum driving might be powerful enough to drive the wind (King 2010b), while at lower luminosities, processes such as line driving and magnetic driving become progressively more important (Proga, Stone & Kallman 2000; Proga 2003; Sim et al. 2008; Fukumura et al. 2010; Higginbottom et al. 2014; Nomura et al. 2016; Cui, Yuan & Li 2020). In these cases, the force multiplier term (the ratio of driving force to the AGN radiation pressure force) depends on several other factors that may differ from one system to another.

Knowledge of outflow properties might provide a way to constrain the origin and physics of UFOs in the near future, when the number of objects with simultaneous UFO and large-scale outflow detections increases. If the spread of UFO kinetic powers is due to variability on short time-scales of decades or less, or a result of different viewing directions, we should also see a large scatter in the correlations between UFO and outflow properties, since outflows react to the long-term energy input by the UFO. Conversely, if UFO differences arise from a diversity of launching mechanisms or efficiencies, then outflow properties might show stronger and less scattered correlations with UFO properties than with AGN luminosity or Eddington ratio.

6.2 Outflow correlations with other galaxy parameters

The variation of AGN luminosity on 10^3–10^6 yr time-scales induces significant scatter in the correlations between outflow parameters and L_{AGN}, as we have shown. However, analytical models (cf. Zubovas & King 2012) predict other correlations between outflow properties and host galaxy parameters, or between separate outflow parameters, that should be preserved and help constrain whether outflows are actually energy driven.

For example, since the energy transferred to the outflow is independent of gas density, we expect outflows in denser systems to be slower, with $v_{out} \propto f_g^{-1/3} \propto M_{gas}^{-1/3}$. This relation is as strong as the dependence on the time-averaged AGN luminosity $\langle L_{AGN} \rangle$: $v_{out} \propto \langle L_{AGN} \rangle^{1/3}$. Therefore, we expect the correlation with M_{gas} to be noticeable even accounting for the scatter induced by AGN luminosity variations.

The mass outflow rate $\dot{M}_{out} \propto f_g v_{out} \propto f_g^{2/3} \propto M_{gas}^{2/3}$ should have an even stronger correlation with gas mass than outflow velocity, therefore the correlation should be even more evident. Of course, the multiphase nature of the gas introduces more scatter into the correlations: since not all the outflowing gas might be detected, and not all the detected gas might be susceptible to AGN wind driving,

the relation between the two quantities may be rather loose. Future observations will improve our understanding of these correlations in two ways: by identifying diffuse gas mass and/or its density and detecting multiple outflow phases; and by determining the radial variation of outflow properties, in a similar way to what has been attempted for Mrk 231 (and Section 4 Feruglio et al. 2015). Although observationally demanding, the full capabilities of *ALMA* have not yet been exploited in the latter sense. The spatial resolution achieved in the *ALMA* observations of PDS 456 and IRAS F11119, for instance, is ∼0.7 and 2.8 kpc, respectively, whereas resolutions of 0.1 kpc or slightly better can be, in principle, reached. Radial profiles of ionized outflows, which can now be obtained for a few nearby Seyferts only (e.g. Crenshaw et al. 2015; Venturi et al. 2018), will be routinely reconstructed in a few years time through integral field spectroscopy with the Extremely Large Telescope. On the other hand, the Square Kilometre Array could eventually reveal the direct radio emission from the shocked wind and ambient gas.

The correlations presented above are technically only valid if the gas and background potential are distributed isothermally. Different radial profiles would affect the correlations, but the qualitative trends should remain the same. It is worth noting that mass outflow rate and outflow velocity should correlate with each other independently of radial density profile or AGN luminosity, and the correlation should only depend on gas mass in the galaxy. Utilizing this correlation might help determine the fraction of total outflowing material that is detected directly and/or the fraction of all gas that is susceptible to joining the outflow.

Finally, there may be a systematic difference between outflows detected close to the nucleus and those seen further away. A single AGN episode may inflate an outflow to a radius $R_1 \sim v_{out}t_{ep} \sim 1 v_{1000}t_{Myr}$ kpc, where t_{Myr} is AGN episode duration in Myr. Given that outflow velocities are usually below 1000 km s^{-1} and durations of individual episodes should not reach 1 Myr, only outflows detected within a few hundred parsecs of the nucleus might be expected to be inflated by the current AGN episode. These outflows might generally be faster for a given galaxy gas content, carry more mass, and show a stronger correlation with the current AGN luminosity than outflows detected further out, where multiple AGN episodes had contributed to their present-day properties. The two outflows in IRAS F11119+3257 reflect these differences rather well, with the inner outflow more easily explained by a model with continuous AGN driving and the outer one requiring intermittent driving (Section 4; see also Nardini & Zubovas 2018). The properties of outflows distant from the nucleus might correlate better with the mass of the SMBH, which sets the maximum, and hence probably the average, AGN luminosity, as found by González-Alfonso et al. (2017); we explore this connection in a companion paper (Nardini & Zubovas, in preparation). We predict that as outflow data becomes better constrained, differences between close-in and distant massive outflows should emerge.

6.3 Constraining AGN luminosity histories and duty cycles

Our results may be useful in inferring the luminosity histories and duty cycles of AGN over the lifetime of an observed outflow, which may be a few times 10^5–10^7 yr. In order to constrain the luminosity history, we can compare the predicted distribution of momentum and/or energy loading factors with the observed distribution in a suitably selected subsample. Our models show that a value of f_{Edd} is a better criterion for selecting the AGN, rather than L_{AGN}. While using the Eddington ratio instead of absolute luminosity requires knowledge of the mass of the SMBH powering the outflow,

thus reducing the available observational sample and introducing additional uncertainty, this choice allows us to investigate loading factor distributions in a physically meaningful way.

The predicted momentum and energy loading factor distributions (Figs 6 and 7) show that every value, up to some maximum, is approximately equally likely to be observed. The maximum value depends on the adopted f_{Edd} threshold and the duty cycle, with lower thresholds and higher duty cycles leading to higher maximum loading factor values. In addition, momentum loading, but not energy loading, depends on host galaxy gas density, with the maximum value $\propto f_g^{1/3}$, as expected from analytical estimates (see Section 6.2). The flatness of these distributions relies on the fact that AGN luminosity decreases approximately as a power law during each episode. If the AGN decayed faster, e.g. exponentially, we would expect many more high loading factors, while if the luminosity stayed at an approximately constant high level for a significant fraction of each episode, we would expect more low loading factors (Zubovas 2018). In principle, then, knowing the distribution of loading factors in a real outflow sample, we can constrain the general shape of the AGN luminosity variation with time.

Real outflows have momentum loading factors that range from well below unity to ∼10^3 (see Table 1), with some fossil outflows having values as large as >10^4 (Fluetsch et al. 2019), however most are clustered in the range $1 < p_{load} < 30$. In this range, the values are distributed mostly uniformly. This allows us to tentatively suggest that most galaxies with known outflows have high gas fractions and/or rather high AGN duty cycles over the outflow lifetime. We refrain from attempting any quantitative estimates because of the rather small sample size.

Assuming that the adopted AGN luminosity prescription is qualitatively correct, we can put constraints on the AGN duty cycle using an individual outflow observation. The average AGN luminosity over a single episode is $L_{ave} \simeq 2.75L_{max}t_q/t_{ep} \simeq 0.057L_{max}$, where the maximum luminosity is probably ∼L_{Edd}. The long-term average AGN luminosity is then $\langle L_{AGN} \rangle \simeq \delta_{AGN}L_{ave} \simeq 0.057\delta_{AGN}L_{Edd}$. Given that the kinetic energy of the outflow is $\dot{E}_{out} \simeq 0.02\langle L_{AGN} \rangle$ (Zubovas & King 2012), we can estimate δ_{AGN}:

$$\dot{E}_{out} \simeq 0.02\langle L_{AGN} \rangle \sim 10^{-3}\delta_{AGN}L_{Edd}; \tag{9}$$

$$\delta_{AGN} \sim 10^3 \frac{\dot{E}_{out}}{L_{Edd}}. \tag{10}$$

This relation is not appropriate for outflows very close to the nucleus, where the outflow properties are dependent on the most recent episode rather than the long-term average (see Section 6.2). For outflows more than a few hundred parsecs away from the nucleus, however, this may be applicable. For these outflows, a high kinetic energy value $\dot{E}_{out}/L_{Edd} > 10^{-3}$ indicates that the AGN was shining essentially continuously while the outflow was expanding, while a lower value indicates a more sporadic AGN history. The individual galaxies we investigated, Mrk 231, PDS 456, and IRAS F11119+3257, have, respectively, $\dot{E}_{out}/L_{Edd} \simeq 6 \times 10^{-3}$, 7×10^{-5}, and 2×10^{-3} (for the outer outflow in the latter two cases). Mrk 231 is clearly consistent with continuous driving by an AGN, with formal $\delta_{AGN} > 5$. On the other hand, PDS 456 requires $\delta_{AGN} \sim 0.07$, very close to the one we used in our model. IRAS F11119+3257 has $\delta_{AGN} = 1.85$, higher than our adopted 0.42, although we also used a higher L_{max} in this case.

It is important to keep in mind that this duty cycle estimate is only applicable for the period during which the outflow has been inflated. An SMBH might grow in 'spurts', periods lasting several tens of Myr (Yu & Tremaine 2002; Hopkins et al. 2005), each composed of many

shorter 'flickering' episodes lasting $\sim 10^5$ yr each. The duty cycle estimate from equation (10) only relates to the period within such a 'spurt'. Over a much longer time-scale comparable to the Hubble time, the duty cycle will be significantly smaller, consistent with observational and theoretical estimates (Wang et al. 2006; Shankar, Weinberg & Miralda-Escudé 2013).

6.4 Multiple spatially distinct outflows

Our model explicitly assumes that the outflow is singular, i.e. there are no spatially distinct components. Physically, this assumption means that the outflow expands through single-phase diffuse ISM without affecting dense clouds, and that those clouds remain dense after the outflow passage and do not refill the cavity left behind. Evidently, this is not always the case: for example, PDS 456 has both a central and an extended outflow component (Bischetti et al. 2019), while IRAS F11119+3257 shows spatially very distinct outflow signatures in OH and CO data (Tombesi et al. 2015; Veilleux et al. 2017). Although alternative interpretations of the data are possible, the plausible existence of separate outflows on different scales must be considered.

Nevertheless, we are confident such a situation should be rare, and most outflows should have only a single spatial component, for the following reason. Consider a galaxy spheroid with a diffuse gas fraction $f_{g, 0}$ and some number of dense clouds. An AGN episode drives a large-scale outflow through the diffuse medium, leaving a cavity behind. The cavity is filled with the shocked AGN wind and has $f_{g, cav} \ll f_{g, 0}$, i.e. it is effectively empty, but overpressurized with respect to the initial ISM pressure. While the AGN episode continues, this shocked wind pressure effectively confines the dense clouds, potentially disrupting them and pushing them away with the diffuse outflow (Hopkins & Elvis 2010) or compressing them leading to enhanced star formation (Zubovas, Sabulis & Naujalis 2014). Once the episode ends, the wind cools down; if the shocked wind is almost adiabatic, cooling happens on the outflow dynamical time-scale $t_d \simeq R_{out}/v_{out} \simeq 10^6 R_{kpc} v_{1000}^{-1}$ yr. At some point, dense clouds are no longer compressed and may evaporate on a time-scale

$$t_{evap} \simeq 5 \times 10^5 R_{pc} T_7^{-5/2} \text{ yr}, \quad (11)$$

where $T_7 \equiv T_{sh}/(10^7 \text{ K})$ is the shocked wind temperature. Here we used the classical evaporation rate for a cloud in hot gas (Cowie & McKee 1977) and the Larson (1981) relations to connect typical cloud density and radius. This is likely a lower limit for the time-scale: most clouds are larger, the wind temperature may well be lower once the clouds are no longer confined, and cloud compression during the AGN episode may lead to them having higher densities than those obtained from Larson relations. Therefore, clouds evaporate rather slowly and increase the diffuse gas density in the outflow cavity to some value $f_{g, 1} < f_{g, 0}$. Even if clouds evaporate rapidly, pressure equilibrium is reached once gas density in the cavity rises to the initial value $f_{g, 0}$, so $f_{g, 1} \leq f_{g, 0}$ always.

Once a new AGN episode begins, the wind encounters gas with, most likely, much lower density than the initial one. The resulting outflow is therefore faster than the (coasting) original outflow, and catches up with the latter on a time-scale shorter than t_d. If several episodes happen in quick succession, the cavity does not refill significantly, and all episodes drive the same outflow. On the other hand, if there is a very long gap between episodes, the fossil outflow may slow down, disperse, and become no longer detectable. This occurs if the AGN is inactive for a period $t_{off} \gtrsim 10 t_{ep}$ (cf. King et al. 2011), i.e. if $\delta_{AGN} < 0.1$ over the several-Myr time-scale. Our estimate of the duty cycle in PDS 456 falls below this threshold,

but not significantly so, therefore this galaxy may be one of the rare cases where the cavity evacuated by the first outflow has been refilled significantly by the time the second outflow started.

If the AGN is observed during the time when the inner outflow has not yet caught up with the outer one, the two outflows should show systematic differences. The inner outflow should be faster but carry less mass than the outer one. It may, however, be more difficult to detect all the mass contained in the outer stalling outflow, especially if its velocity is currently similar to the velocity dispersion and/or rotational velocity of other gas in the galaxy.

The above picture is complicated by the presence of coherent structures feeding the SMBH via gravitational torques (e.g. Anglés-Alcázar et al. 2017). They may continuously refill the outflow cavity faster than evaporating clouds do, leading to separate AGN episodes acting on distinct gas reservoirs and producing separate outflows. This situation is particularly relevant for gas-rich mergers, which are common hosts of AGN-driven outflows.

6.5 Multiphase outflows

The outflowing gas can be ionized by shocks and by the AGN radiation field, and cools down mainly via bremsstrahlung, metal line, and atomic cooling processes. The effect of shocks depends primarily on the outflow velocity and so remains almost constant as the outflow evolves. However, the much more abrupt changes in AGN luminosity can have significant effects on the ionization state of the outflow. Even in the presence of the AGN radiation field, the outflow can cool and form molecules (Zubovas & King 2014; Richings & Faucher-Giguère 2018a,b). Higher AGN luminosity results in slower cooling, with $L_{AGN} = 10^{45}$ erg s^{-1} leading to molecule formation on a time-scale of $t_{form} \simeq 0.3$ Myr, while for $L_{AGN} = 10^{46}$ erg s^{-1}, $t_{form} \simeq 0.6$ Myr, at least in models with constant ISM density $n_H = 10$ cm^{-3} (Richings & Faucher-Giguère 2018a,b). These time-scales are longer than the duration of individual AGN episodes estimated via observational (Schawinski et al. 2015) and analytical (King & Nixon 2015) arguments, therefore we may expect the ratio of molecular and atomic/ionized gas in outflows in real galaxies to be the result of a complex interplay of time-dependent heating and cooling processes. Evidently, at higher luminosity, the importance of heating increases: in AGN with $L_{AGN} = 10^{45}$ erg s^{-1}, ionized mass outflow rates are ~ 0.01 times the molecular ones, but the ratio increases to > 0.1 for AGN with $L_{AGN} = 10^{46}$ erg s^{-1} (Fiore et al. 2017; Bischetti et al. 2019).

Qualitatively, this trend is easy to understand. When the AGN switches on, the heating rate increases significantly on a light traveltime. Meanwhile, the cooling rate hardly changes, since outflow properties change very little over the course of a single episode, assuming that the outflow has been expanding for a few episodes already. As the AGN luminosity decays and especially when the episode ends, the ionization balance changes and may lead to the ionized gas disappearing completely. The recombination time in the comparatively dense outflow is much shorter than in the undisturbed ISM or circumgalactic medium (CGM) (Zubovas & King 2014), so we would not expect long-lived ionized remnants to be present in the outflow. Formation of molecules from the recently cooled material takes some time, so fossil outflows might trace only the molecular component of the original outflow. This situation may result in ionized outflows having stronger correlations with L_{AGN} than molecular ones, simply because their detection is affected by the AGN more strongly than that of molecular gas. We plan to explore these correlations in more detail in a future publication.

6.6 Implementation in numerical simulations

Numerical simulations of galaxy evolution often include AGN feedback in the form of energy injection into gas surrounding the SMBH particle (e.g. Sijacki et al. 2007; Vogelsberger et al. 2014; Schaye et al. 2015; Tremmel et al. 2019). Currently, these simulations reach spatial and temporal resolution that is comparable to the accreted mass and duration of individual AGN episodes (Grand et al. 2017; Nelson et al. 2019; Tremmel et al. 2019). This presents an opportunity to upgrade the AGN feedback prescription in order to achieve more realistic galaxy behaviour. Two ingredients are necessary for this upgrade.

First of all, SMBH feeding is typically unresolved, with a Bondi–Hoyle-like prescription used to estimate the accretion rate (Booth & Schaye 2009). As the mass, if not spatial, resolution reaches values low enough to accommodate the growth of an accretion disc around the SMBH (i.e. $m_{\rm res} \ll M_{\rm BH}$), introducing a subresolution prescription for disc evolution should give more realistic time evolution of the SMBH feeding rate and hence the variation of AGN luminosity. In particular, the accretion disc particle method (Power, Nayakshin & King 2011) can reproduce realistic AGN behaviour which has little dependence on the free parameters of the model (Wurster & Thacker 2013). This prescription should be able to reproduce the AGN flickering behaviour on 10^4–10^5 yr time-scales (King & Nixon 2015; Schawinski et al. 2015), which in turn produces realistic distributions of outflow loading factors (see also Zubovas 2018).

The second improvement would be to adopt a more realistic geometry of feedback energy injection. Depositing the energy into some number of nearest particles to the SMBH results in dense gas close to the SMBH absorbing a disproportionately large amount of energy, leading to weak outflows and unphysical stalling of SMBH growth (Zubovas et al. 2016); this can be alleviated if energy is injected into a bicone. Using such a prescription would create more realistic dynamics of AGN feeding reservoirs and allow prolonged AGN growth periods that might contain numerous flickering episodes.

This approach would help make simulations more realistic on the level of individual galaxies and processes happening therein. Such simulations could be checked and constrained by the growing data set of observed AGN-driven outflows. Furthermore, they would help investigate the relationship between outflow parameters and the properties of their host galaxies and/or broader environment.

7 SUMMARY AND CONCLUSION

We numerically investigated the evolution of galactic outflows driven by intermittent AGN episodes each lasting $\sim 10^4$–10^5 yr, with particular emphasis on how this luminosity evolution affects the observable momentum and energy loading factors. We considered three individual galaxies – Mrk 231, PDS 456, and IRAS F11119+3257 (Section 4) – and a distribution of loading factors seen in several tens of other outflows (Section 5). The main results are the following:

(i) The outflow in Mrk 231, which shows a momentum loading factor of $\dot{p}_{\rm out} c / L_{\rm AGN} > 5$ and an energy loading factor $\dot{E}_{\rm out} / L_{\rm AGN} > 0.006$ (for the molecular component; both loading factors are presumably a factor ~ 2 greater when the neutral gas outflow is taken into account), can be adequately explained as an almost spherically symmetric energy-driven outflow expanding under continuous driving by the AGN for the past $t_{\rm out} \sim 1$ Myr.

(ii) Conversely, the 'unexpectedly weak' outflow in PDS 456 is not compatible with continuous driving at the present-day AGN luminosity, but can be explained using a model where the AGN luminosity varies in time with a duty cycle $\delta_{\rm AGN} = 0.084$; in this case, the present-day luminosity is much higher than the long-term average.

(iii) The outflow in IRAS F11119+3257 is an intermediate case: the 300-pc-scale outflow can be explained by a continuous-luminosity model, while the intermittent AGN model, with a duty cycle $\delta_{\rm AGN} = 0.42$, is a better fit to the 7-kpc-scale one.

(iv) For a population of AGN outflows observed at random times in their evolution, the distribution of observed momentum and energy loading factors does not depend on SMBH or galaxy mass, but only on the AGN duty cycle, gas density, and the threshold $f_{\rm Edd}$ for AGN selection;

(v) Assuming that AGN are selected because of bright thin-disc emission, i.e. $f_{\rm Edd} > 0.01$, a small, but non-negligible fraction of outflows should have low momentum and energy loading factors: $p_{\rm load} < 1$ in 5–15 per cent of cases in models with low AGN duty cycle $\delta_{\rm AGN} = 0.084$, depending on gas density, with higher density leading to lower probability of observing small loading factors.

(vi) The fraction of outflows with small loading factors increases significantly if only AGN with $f_{\rm Edd} > 0.1$ are considered ($p_{\rm load} < 1$ in 60–95 per cent of cases) and decreases if the AGN duty cycle is higher ($p_{\rm load} < 1$ in 2–6 per cent of cases when $\delta_{\rm AGN} = 0.42$).

These results show that a lot of the observed variation among AGN-driven outflows may simply be the outcome of AGN luminosity varying significantly with time. As more observational data is collected and as numerical simulation resolution steadily improves, the evolution of individual AGN outflows, as well as AGN luminosity histories over the past several Myr, should become traceable, greatly enhancing our understanding of the coevolution of SMBHs and their host galaxies.

DATA AVAILABILITY

Observational data used in this paper is presented in Section 3 and Table 1; it is taken from publicly available sources. The code used for the modelling is currently being prepared for public release; for the moment, it is available upon reasonable request to the corresponding author.

REFERENCES

Aalto S., Muller S., Sakamoto K., Gallagher J. S., Martín S., Costagliola F., 2012, A&A, 546, A68
Anglés-Alcázar D., Davé R., Faucher-Giguère C.-A., Özel F., Hopkins P. F., 2017, MNRAS, 464, 2840
Barcos-Muñoz L. et al., 2018, ApJ, 853, L28
Bentz M. C. et al., 2013, ApJ, 767, 149
Best P. N., Heckman T. M., 2012, MNRAS, 421, 1569
Bischetti M. et al., 2019, A&A, 628, A118
Bolatto A. D., Wolfire M., Leroy A. K., 2013a, ARA&A, 51, 207
Bolatto A. D. et al., 2013b, Nature, 499, 450
Booth C. M., Schaye J., 2009, MNRAS, 398, 53
Bourne M. A., Nayakshin S., 2013, MNRAS, 436, 2346
Bower R. G., Benson A. J., Malbon R., Helly J. C., Frenk C. S., Baugh C. M., Cole S., Lacey C. G., 2006, MNRAS, 370, 645

Cicone C., Feruglio C., Maiolino R., Fiore F., Piconcelli E., Menci N., Aussel H., Sturm E., 2012, A&A, 543, A99

Cicone C. et al., 2014, A&A, 562, A21

Cicone C. et al., 2018, ApJ, 863, 143

Combes F. et al., 2013, A&A, 558, A124

Costa T., Rosdahl J., Sijacki D., Haehnelt M. G., 2018, MNRAS, 473, 4197

Cowie L. L., McKee C. F., 1977, ApJ, 211, 135

Crenshaw D. M., Fischer T. C., Kraemer S. B., Schmitt H. R., 2015, ApJ, 799, 83

Croton D. J. et al., 2006, MNRAS, 365, 11

Cui C., Yuan F., Li B., 2020, ApJ, 890, 80

Dasyra K. M., Combes F., 2011, A&A, 533, L10

Downes D., Solomon P. M., 1998, ApJ, 507, 615

Dubois Y. et al., 2014, MNRAS, 444, 1453

Faucher-Giguère C.-A., Quataert E., 2012, MNRAS, 425, 605

Feruglio C., Maiolino R., Piconcelli E., Menci N., Aussel H., Lamastra A., Fiore F., 2010, A&A, 518, L155+

Feruglio C., Fiore F., Piconcelli E., Cicone C., Maiolino R., Davies R., Sturm E., 2013, A&A, 558, A87

Feruglio C. et al., 2015, A&A, 583, A99

Fiore F. et al., 2017, A&A, 601, A143

Fluetsch A. et al., 2019, MNRAS, 483, 4586

Fukumura K., Kazanas D., Contopoulos I., Behar E., 2010, ApJ, 715, 636

García-Burillo S. et al., 2014, A&A, 567, A125

García-Burillo S. et al., 2015, A&A, 580, A35

Giustini M., Proga D., 2019, A&A, 630, A94

Gofford J., Reeves J. N., Tombesi F., Braito V., Turner T. J., Miller L., Cappi M., 2013, MNRAS, 430, 60

González-Alfonso E. et al., 2017, ApJ, 836, 11

Gowardhan A. et al., 2018, ApJ, 859, 35

Grand R. J. J. et al., 2017, MNRAS, 467, 179

Hamann F., Chartas G., Reeves J., Nardini E., 2018, MNRAS, 476, 943

Harrison C. M., Costa T., Tadhunter C. N., Flütsch A., Kakkad D., Perna M., Vietri G., 2018, Nat. Astron., 2, 198

Heckman T. M., Best P. N., 2014, ARA&A, 52, 589

Higginbottom N., Proga D., Knigge C., Long K. S., Matthews J. H., Sim S. A., 2014, ApJ, 789, 19

Hopkins P. F., Elvis M., 2010, MNRAS, 401, 7

Hopkins P. F., Hernquist L., Martini P., Cox T. J., Robertson B., Di Matteo T., Springel V., 2005, ApJ, 625, L71

Ishibashi W., Fabian A. C., 2015, MNRAS, 451, 93

King A., 2003, ApJ, 596, L27

King A., 2005, ApJ, 635, L121

King A., Nixon C., 2015, MNRAS, 453, L46

King A., Pounds K., 2015, ARA&A, 53, 115

King A. R., 2010a, MNRAS, 402, 1516

King A. R., 2010b, MNRAS, 408, L95

King A. R., Pounds K. A., 2003, MNRAS, 345, 657

King A. R., Pringle J. E., 2007, MNRAS, 377, L25

King A. R., Zubovas K., Power C., 2011, MNRAS, 415, L6

Larson R. B., 1981, MNRAS, 194, 809

Leon S. et al., 2007, A&A, 473, 747

Lutz D. et al., 2020, A&A, 633, A134

Maiolino R. et al., 2012, MNRAS, 425, L66

Matthews J. H., Knigge C., Long K. S., Sim S. A., Higginbottom N., Mangham S. W., 2016, MNRAS, 458, 293

Matzeu G. A., Reeves J. N., Nardini E., Braito V., Costa M. T., Tombesi F., Gofford J., 2016, MNRAS, 458, 1311

Matzeu G. A., Reeves J. N., Braito V., Nardini E., McLaughlin D. E., Lobban A. P., Tombesi F., Costa M. T., 2017, MNRAS, 472, L15

McConnell N. J., Ma C.-P., 2013, ApJ, 764, 184

Morganti R., Frieswijk W., Oonk R. J. B., Oosterloo T., Tadhunter C., 2013, A&A, 552, L4

Murray N., Quataert E., Thompson T. A., 2005, ApJ, 618, 569

Nardini E., Zubovas K., 2018, MNRAS, 478, 2274

Nardini E. et al., 2015, Science, 347, 860

Navarro J. F., Frenk C. S., White S. D. M., 1997, ApJ, 490, 493

Nelson D. et al., 2019, MNRAS, 490, 3234

Nims J., Quataert E., Faucher-Giguère C.-A., 2015, MNRAS, 447, 3612

Nomura M., Ohsuga K., Takahashi H. R., Wada K., Yoshida T., 2016, PASJ, 68, 16

Papadopoulos P. P., van der Werf P., Xilouris E., Isaak K. G., Gao Y., 2012, ApJ, 751, 10

Pereira-Santaella M. et al., 2016, A&A, 594, A81

Pereira-Santaella M. et al., 2018, A&A, 616, A171

Pounds K. A., King A. R., 2013, MNRAS, 433, 1369

Pounds K. A., Reeves J. N., King A. R., Page K. L., O'Brien P. T., Turner M. J. L., 2003, MNRAS, 345, 705

Pounds K., Lobban A., Reeves J., Vaughan S., 2016, MNRAS, 457, 2951

Power C., Nayakshin S., King A., 2011, MNRAS, 412, 269

Proga D., 2003, ApJ, 585, 406

Proga D., Stone J. M., Kallman T. R., 2000, ApJ, 543, 686

Puchwein E., Springel V., 2013, MNRAS, 428, 2966

Querejeta M. et al., 2016, A&A, 593, A118

Reeves J. N., Braito V., 2019, ApJ, 884, 80

Reeves J. N., O'Brien P. T., Ward M. J., 2003, ApJ, 593, L65

Reeves J. N., Lobban A., Pounds K. A., 2018a, ApJ, 854, 28

Reeves J. N., Braito V., Nardini E., Lobban A. P., Matzeu G. A., Costa M. T., 2018b, ApJ, 854, L8

Reeves J. N., Braito V., Chartas G., Hamann F., Laha S., Nardini E., 2020, ApJ, 895, 37

Richards G. T. et al., 2006, ApJS, 166, 470

Richings A. J., Faucher-Giguère C.-A., 2018a, MNRAS, 474, 3673

Richings A. J., Faucher-Giguère C.-A., 2018b, MNRAS, 478, 3100

Roberts-Borsani G. W., 2020, MNRAS, 494, 4266

Rupke D. S. N., Veilleux S., 2011, ApJ, 729, L27

Rupke D. S., Veilleux S., Sanders D. B., 2005, ApJS, 160, 115

Rupke D. S. N., Gültekin K., Veilleux S., 2017, ApJ, 850, 40

Sakamoto K., Aalto S., Combes F., Evans A., Peck A., 2014, ApJ, 797, 90

Salak D., Nakai N., Hatakeyama T., Miyamoto Y., 2016, ApJ, 823, 68

Schawinski K., Koss M., Berney S., Sartori L. F., 2015, MNRAS, 451, 2517

Schaye J. et al., 2015, MNRAS, 446, 521

Shankar F., Weinberg D. H., Miralda-Escudé J., 2013, MNRAS, 428, 421

Sijacki D., Springel V., Di Matteo T., Hernquist L., 2007, MNRAS, 380, 877

Sim S. A., Long K. S., Miller L., Turner T. J., 2008, MNRAS, 388, 611

Simpson C., Ward M., O'Brien P., Reeves J., 1999, MNRAS, 303, L23

Sirressi M. et al., 2019, MNRAS, 1927, 489

Smith R. N., Tombesi F., Veilleux S., Lohfink A. M., Luminari A., 2019, ApJ, 887, 69

Sturm E. et al., 2011, ApJ, 733, L16

Sun A.-L., Greene J. E., Zakamska N. L., Nesvadba N. P. H., 2014, ApJ, 790, 160

Sądowski A., Narayan R., Penna R., Zhu Y., 2013, MNRAS, 436, 3856

Tombesi F., Cappi M., Reeves J. N., Palumbo G. G. C., Yaqoob T., Braito V., Dadina M., 2010a, A&A, 521, A57+

Tombesi F., Sambruna R. M., Reeves J. N., Braito V., Ballo L., Gofford J., Cappi M., Mushotzky R. F., 2010b, ApJ, 719, 700

Tombesi F., Cappi M., Reeves J. N., Braito V., 2012, MNRAS, 422, L1

Tombesi F., Cappi M., Reeves J. N., Nemmen R. S., Braito V., Gaspari M., Reynolds C. S., 2013, MNRAS, 430, 1102

Tombesi F., Tazaki F., Mushotzky R. F., Ueda Y., Cappi M., Gofford J., Reeves J. N., Guainazzi M., 2014, MNRAS, 443, 2154

Tombesi F., Meléndez M., Veilleux S., Reeves J. N., González-Alfonso E., Reynolds C. S., 2015, Nature, 519, 436

Torres C. A. O., Quast G. R., Coziol R., Jablonski F., de la Reza R., Lépine J. R. D., Gregório-Hetem J., 1997, ApJ, 488, L19

Tremmel M. et al., 2019, MNRAS, 483, 3336

Tsai A.-L. et al., 2009, PASJ, 61, 237

Tsai A.-L., Matsushita S., Kong A. K. H., Matsumoto H., Kohno K., 2012, ApJ, 752, 38

Veilleux S. et al., 2009, ApJS, 182, 628

Veilleux S., Bolatto A., Tombesi F., Meléndez M., Sturm E., González-Alfonso E., Fischer J., Rupke D. S. N., 2017, ApJ, 843, 18

Venturi G. et al., 2018, A&A, 619, A74

Vogelsberger M. et al., 2014, MNRAS, 444, 1518

Walter F., Weiss A., Scoville N., 2002, ApJ, 580, L21
Wang J.-M., Chen Y.-M., Zhang F., 2006, ApJ, 647, L17
Wurster J., Thacker R. J., 2013, MNRAS, 431, 539
Yu Q., Tremaine S., 2002, MNRAS, 335, 965
Zheng X. Z., Xia X. Y., Mao S., Wu H., Deng Z. G., 2002, AJ, 124, 18
Zschaechner L. K. et al., 2016, ApJ, 832, 142
Zubovas K., 2018, MNRAS, 473, 3525
Zubovas K., 2019, MNRAS, 483, 1957

Zubovas K., King A., 2012, ApJ, 745, L34
Zubovas K., King A. R., 2014, MNRAS, 439, 400
Zubovas K., King A., 2016, MNRAS, 462, 4055
Zubovas K., Sabulis K., Naujalis R., 2014, MNRAS, 442, 2837
Zubovas K., Bourne M. A., Nayakshin S., 2016, MNRAS, 457, 496

This paper has been typeset from a TEX/LATEX file prepared by the author.